Formation and protection of an Eu-Ir surface compound below hexagonal boron nitride

Applied Surface Science 746 (2026) 167568

Contents lists available at ScienceDirect

Applied Surface Science

journal homepage: www.elsevier.com/locate/apsusc

Full length article

Formation and protection of an Eu-Ir surface compound below hexagonal boron nitride

Alaa Mohammed Idris Bakhit [a,b,c,*], Khadiza Ali [a,d,e], Anna A. Makarova [f], Frederik Schiller [a,**]

[a] Centro de Física de Materiales (CSIC-UPV-EHU) and Materials Physics Center (MPC), 20018 San Sebastián, Spain
[b] Departamento de Física Aplicada I, Universidad del País Vasco UPV/EHU, 20018 San Sebastián, Spain
[c] Donostia International Physics Center (DIPC), 20018 Donostia-San Sebastián, Spain
[d] Chalmers University of Technology, Göteborg, Chalmersplatsen 4, 412 96 Göteborg, Sweden
[e] Department of Physics, BITS Pilani, Hyderabad Campus, Hyderabad, 500078, Telangana, India
[f] Helmholtz-Zentrum Berlin für Materialien und Energie, Elektronenspeicherring BESSY II, Albert-Einstein-Str. 15, 12489 Berlin, Germany

ARTICLE INFO

Keywords:
Hexagonal boron nitride
Eu intercalation
Ambient conditions and X-ray photoelectron spectroscopy (XPS)

ABSTRACT

The intercalation of europium (Eu) offers an opportunity to tailor magnetic and electronic properties at interfaces, yet its behavior beneath protective 2D overlayers remains poorly understood. Here, Eu intercalation below a monolayer of hexagonal boron nitride (hBN) on Ir(111) was systematically investigated by varying the Eu deposited amount and substrate temperature. Eu was chosen for its tunable valence state and potential for ferromagnetic ordering. The structural and electronic properties were examined using low-energy electron diffraction (LEED), scanning tunneling microscopy (STM), X-ray photoelectron spectroscopy (XPS), and angle-resolved photoemission spectroscopy (ARPES). Three superstructures were identified with respect to Ir(111) substrate by LEED: $(5 \times M)$ superstructure at 0.12 ML surface coverage, preserving the hBN/Ir(111) Moiré pattern with unidirectional Eu ordering; (5×2) superstructure at 0.9 ML where excess Eu adopts a tri-valent state and forms an alloy with Ir; and $(\sqrt{3}\times\sqrt{3})R30°$ superstructure at the highest preparation temperature and 0.3 ML consistent with 2D surface phase $EuIr_2$ alloy formation with di-valent Eu. The intercalation pathway is attributed to grain boundaries and structural defects in the hBN overlayer, emphasizing hBN quality in controlling intercalation. The protective role of the hBN layer was evaluated by air exposure, resulting in a 20% protection.

1. Introduction

2D materials grown on metal substrates [1,2] have attracted significant attention due to their unique electronic properties and potential applications in nanoelectronics and spintronics. Among these, the intercalation of metals [3] beneath these materials has emerged as a promising approach to tuning the electronic and magnetic properties of these systems [4]. Additionally, 2D materials can serve as a protective layer, shielding underlying materials from ambient conditions. For example, graphene [5–12] and hBN [13–21] were used as protection layers.

Specifically, rare-earth metals are very reactive and oxidize easily under ambient conditions. Europium belongs to this group of metals and is considered the most reactive one [22]. In a solid compound, Eu may exhibit di-valent, tri-valent or even a mixed-valent state [23–25]. The di-valent state has ferromagnetic properties, making Eu promising for spintronics applications. However, Eu is highly reactive in air, limiting its practical use. Under such conditions, Eu will oxidize to the tri-valent Eu_2O_3, which is not ferromagnetic.

The intercalation of Eu atoms beneath layered materials has been investigated mainly for graphite and graphene [11,12,26–30] and more recently below the hBN monolayer [20,21,31]. Nevertheless, not much attention was paid to the stability of Eu in such intercalation systems.

In addition to the previously reported Eu intercalation below the hBN on Pt(111) system, a newly published study examined the Eu intercalation beneath hBN on Ni(111) [21]. The intercalation of Eu under the graphene/Ir(111) or hBN/Pt(111) systems gave rise to europium atoms with ferromagnetic behavior that depends on the amount of Eu intercalated [20,28]. In the former system, a (2×2) superstructure formed where the Eu–Eu distance doubles the Ir interatomic distance

* Corresponding author at: Centro de Física de Materiales (CSIC-UPV-EHU) and Materials Physics Center (MPC), 20018 San Sebastián, Spain.
** Corresponding author.
E-mail addresses: alaa.mohammed@dipc.org (A. Mohammed Idris Bakhit), frederikmichael.schiller@ehu.es (F. Schiller).

https://doi.org/10.1016/j.apsusc.2026.167568
Received 24 February 2026; Received in revised form 23 April 2026; Accepted 15 June 2026
Available online 22 June 2026

of the (111) face, amounting approx. 5.4 Å. There, Eu atoms have a paramagnetic state [28]. When the Eu atoms arrange in a $(\sqrt{3} \times \sqrt{3})R30°$ superstructure corresponding to approx. 4.7 Å Eu-Eu distance, ferromagnetic behavior on Ir and Pt is obtained [20,28].

The origin of the different magnetic properties was assigned mainly to the RKKY-type interaction between the Eu atoms mediated by valence band electrons of the substrate. On the one hand, the distance between Eu atoms is one of the crucial parameters for the magnetic interaction; on the other hand, the influence of the valence bands of the Ir, Pt or Rh atoms is important [20,28,32]. For the Eu-Ir bulk compounds, $EuIr_2$ attracted the most attention in the late sixties of the last century as an initially described ferromagnetic compound [33]; nevertheless, the magnetic susceptibility did not correspond to Eu^{3+}, the valence state of its constituents [34]. Only one year later, the discovery of EuO as a ferromagnetic compound resolved the puzzle, with the possible contamination of the latter being responsible for the previously observed ferromagnetic behavior in $EuIr_2$ [35,36] while pure $EuIr_2$ has tri-valent Eu atoms [37].

Interestingly, later $EuIr_2$ compound was found to be superconducting [38], confirming europium atoms in a tri-valent state. Furthermore, Eu in other bulk materials can exist with intermediate valence [39], either due to different crystallographic Eu sites as in Eu_3O_4 [40], due to valent fluctuating system as in $EuIr_2Si_2$ [41] or due to non-integer Eu valence in intermediate valent systems that originate from hybridization between the 4f moments and the conduction electrons as in $EuCu_2(Si_xGe_{1-x})_2$ [24]. A last aspect to mention is that on the surface, however, nearly all Eu or Sm compounds are di-valent [42,43]. For the Eu-Ir system considered in this work, only bulk $EuIr_2$ is well characterized, in the latter case as one of the scarce tri-valent Eu compounds [44]. However, also in such a case, the Eu atoms at the surface are expected to be di-valent.

In this context, our study investigates the intercalation of Eu atoms beneath a monolayer of hBN on an Ir(111) substrate. By systematically varying the Eu deposited amount and deposition conditions of Eu, we aim to uncover the structural and electronic transformations that occur. Employing characterization techniques such as Low Energy Electron Diffraction (LEED), Scanning Tunneling Microscopy (STM), X-ray Photoelectron Spectroscopy (XPS), and Angle-Resolved Photoemission Spectroscopy (ARPES), we provide a comprehensive analysis of the impact of Eu intercalation. Our findings reveal the formation of distinct superstructures, including $(5 \times M)$, (5×2), and $(\sqrt{3} \times \sqrt{3})R30°$ depending on Eu coverage and deposition temperature ($M > 2$). At surface coverage of 0.12 monolayer (ML), the $(5 \times M)$ superstructure preserves the hBN/Ir Moiré pattern with the unidirectional ordering of the Eu atoms. Increasing the surface coverage leads to a (5×2) superstructure, with excess Eu atoms diffusing into the bulk as tri-valent Eu. At surface saturation coverage and slightly higher substrate temperature during deposition, the formation of a $(\sqrt{3} \times \sqrt{3})R30°$ superstructure indicates the presence of a 2D surface phase $EuIr_2$ alloy beneath the hBN layer, where di-valent Eu suggests potential ferromagnetic properties. Moreover, we assess the protective role of the hBN layer against air exposure, finding that the 2D surface phase $EuIr_2$ alloy is around 20% partially protected. This investigation advances our understanding of Eu intercalation beneath hBN on Ir(111) and highlights the potential for developing new 2D ferromagnetic materials with tailored electronic and magnetic properties for practical use in spintronics applications.

2. Experimental methods

The Ir(111) single crystal (Mateck GmbH) was cleaned using multiple cycles of Argon ion sputtering (1.3 kV) at a pressure of $3 \cdot 10^{-6}$ mbar at room temperature, followed by an annealing to 950 K. Occasionally, the sample was heated in an oxygen atmosphere at $5 \cdot 10^{-8}$ mbar to remove carbon impurities, maintaining a temperature of 1120 K for 5 min, then flash-annealing to 1200 K for 4 min.

The synthesis of hBN on Ir(111) was achieved using the Chemical Vapor Deposition (CVD) technique. For this purpose, a clean Ir(111) substrate was heated and exposed to borazine precursor ($B_3H_6N_3$, KATCHEM spol. s r.o.) for 12 min at a pressure of $5 \cdot 10^{-7}$ mbar. These parameters are used in all experiments presented here, where hBN was grown with the substrate maintained at temperatures between 1120 K and 1220 K.

Eu intercalation beneath the hBN on Ir(111) was carried out at different temperatures and Eu coverages: 800 K (0.12 ML), 920 K (0.9 ML), and 940 K (0.3 ML). Further in the text, the ML amount will be defined in detail. It will be shown that the superstructure is defined by the substrate temperature, not by the Eu coverage, since the exceeding Eu will diffuse into the Ir bulk. Subsequent experiments were conducted to investigate the protection from oxidation. This was achieved through two methods: first, by directly exposing the sample to 1000 L of oxygen for 5 min; and second, by subjecting the sample to ambient pressure conditions (room temperature, 80% humidity) for 5 min. In both cases, followed by annealing to T_{Sample}=745 K and T_{Sample}=506 K, respectively.

Experiments were conducted under ultra-high vacuum (UHV) conditions at the Material Physics Center (MPC) in San Sebastian, Spain, maintaining a base pressure of $5 \cdot 10^{-10}$ mbar or less. Characterization of both structural and electronic properties encompassed a comprehensive array of techniques, including LEED, STM, ARPES, and XPS. LEED measurements utilized the conventional three-grid design from Omicron equipment. STM measurements were conducted in constant current mode using an Omicron VT-STM microscope, with image analysis processed via the WSXM program [45]. Both techniques were performed at room temperature. Additionally, XPS spectra were obtained using a Specs Al K_α μ-FOCUS 600 monochromator at $h\nu$ = 1486.6 eV. ARPES measurements were carried out using a Specs UVS-300 discharge lamp with Specs TMM 304 monochromator utilizing He IIα light at a photon energy of 40.8 eV. Electron detection was performed with a SPECS Phoibos 150 analyzer, configured for 200 meV energy and 2° angular resolution. Spectroscopic experiments were again performed at room temperature. Furthermore, the deposition of 0.1 ML Eu into a clean Ir(111) substrate experiment was investigated employing photoemission spectroscopy at the GELEM Dipole beamline at the BESSY II electron storage ring operated by the Helmholtz-Zentrum Berlin für Materialien und Energie [46] in Berlin, Germany. XPS spectra were acquired with a Phoibos-150 electron energy analyzer.

3. Eu/Ir(111) interface

As already mentioned and verified in the example of EuO contamination on $EuIr_2$, the protection of rare-earth metals in their metallic form is a major issue. To address the protection problem related to the very reactive rare-earth metals, first, the chemical properties of Eu deposited on an Ir(111) substrate in ultra-high vacuum conditions were analyzed by X-ray photoemission spectroscopy. Three experiments were conducted under different deposition conditions [32], see Tab. S1 in supplemental material (SM) [47] for experimental parameters. First, Eu was deposited during 15 min at T_{sample} = 930 K, a temperature in the range used in our work to intercalate Eu beneath hBN on Ir(111). Neither a superstructure was observed in LEED nor was Eu detected in the XPS survey spectra (see Fig. S1 in the SM [47]). This suggests that the deposited Eu does not remain on the surface but instead re-evaporates, preventing any stable Eu overlayer formation or even Eu incorporation into the Ir first layer. It is important to note that when the hBN layer is present, Eu atoms intercalate beneath hBN at this high temperature, preventing their re-evaporation and leading to Eu diffusion into the bulk when the surface is saturated. Next, the temperature was reduced to 630 K and Eu was deposited the same 15 min as in the previous case on clean Ir(111). Neither here a different LEED pattern appeared, although Eu was clearly detected in the XPS survey (Fig. S2 in the SM [47]). The Eu coverage was estimated from the core level intensities

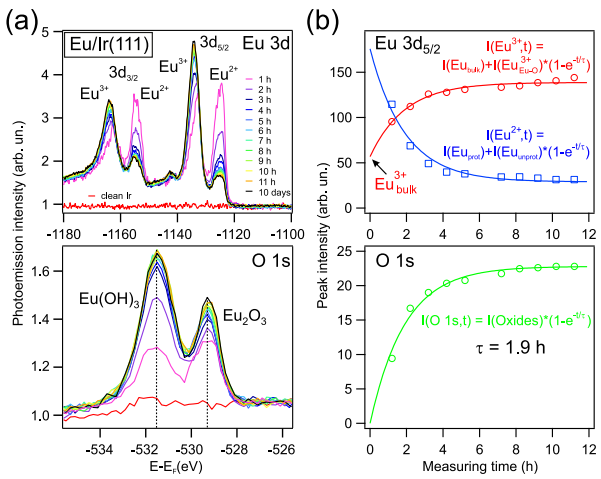

Fig. 1. XPS analysis of approx. 1 ML Eu deposited onto Ir(111) crystal. (a) Eu 3d and O 1s X-ray photoemission spectra were obtained using Al K_α radiation with the sample kept in Ultra-High Vacuum (UHV) conditions. Oxidation occurred with the rest gas atoms in UHV. (b) Analysis of the peak intensities from the fitted spectra of (a). The solid lines are exponential fits of the peak areas as indicated in the equations. The lifetime τ resulted from the fit of the O 1s intensities (Eu_2O_3 and hydroxide) and was then applied to the Eu^{2+} and Eu^{3+} peaks. Back-tracing of the time evolution by using τ to the Eu components as indicated in (b) results in an initial content of approx. 1/4 of Eu in a tri-valent state.

of Eu 3d and the decay of the Ir 4f intensity to be 0.15 ML, where an ML here is a complete Eu surface. The experiment was repeated with a $T_{sample} = 630$ K and a higher Eu coverage of approx. 1 ML to allow for a more systematic study, particularly of Eu oxidation over time. This amount was sufficient to achieve a (2 × 2) superstructure in LEED, the corresponding XPS survey is shown in Fig. S3 in the SM [47], which clearly revealed the presence of Eu 3d core-level features with mixed-valence character. Following the initial survey scan, time-resolved XPS measurements (see Fig. 1) were carried out to inspect the oxidation process in detail, specifically by tracking the evolution of the Eu 3d and O 1s core-level spectra as a function of time. The base pressure of the vacuum chamber during this experiment was $p = 3 \cdot 10^{-10}$mbar. Eu presented a mixture of valence states, namely di-valent and tri-valent Eu with binding energies of the leading $3d_{5/2}$ peaks at approx. $E - E_F = -1125.6$ eV and −1134.7 eV, respectively. The presence of di-valent Eu at the surface, either as a result of an Eu-Ir surface alloy or due to individual Eu atoms at the surface, is detected. The tri-valent Eu emission may arise either from oxidized Eu_2O_3, $Eu(OH)_3$, or from Eu atoms that diffuse into the bulk. Careful inspection of the peak form and energy reveals a change in that Eu^{3+} emission, pointing to the fact that at the beginning, Eu with a different environment is observed. On the other side, the corresponding O 1s spectra exhibit two main components: Eu-OH, or more specifically $Eu(OH)_3$, at higher and Eu_2O_3 at lower binding energies, as found for bulk Eu_2O_3 samples [48,49]. Additionally, a minor component corresponding to the adsorbed water was determined from the fit shown in the SM [47] in Fig. S4. Tri-valent Eu and O 1s increase with time, while the di-valent Eu contribution diminishes. One can fit the time evolution of the total O 1s intensity with an exponential curve by assuming that no oxide is formed at deposition ($t = 0$). This means that the Eu atoms at the surface oxidizes with the rest vacuum by

$$I(t) = I_{tot} \cdot \left(1 - e^{-t/\tau}\right). \quad (1)$$

being I_{tot} the O 1s intensity of the total oxide formed. The only fitting parameter, τ, is the mean lifetime of the di-valent Eu atoms at the surface and resulted in $\tau = (1.9 \pm 0.5)$ hours (h). Within this approx. 2 h time frame and taking into account the base pressure, one would accumulate 1.5 L of rest gas dosage on the sample and due to the high reactivity of Eu, oxidation and formation of the tri-valent Eu takes place. This mean lifetime τ can be used to back trace the initial amounts of tri-valent Eu right after deposition. With the formula indicated in Fig. 1, we estimate that initially approx. a quarter of the Eu was already in tri-valent state. Such Eu^{3+} would not exist for pure Eu, which is di-valent, but can only be formed due to Eu diffusion into the Ir bulk during the preparation at 630 K. This is supported by the results shown in Fig. S5 in the SM [47], where 0.1 ML Eu was deposited on a clean Ir substrate. Such enhanced Eu interdiffusion is also known for Ir neighboring elements Pt [20] or Pd [50], in the latter case even at 77 K. Apart from the Eu interdiffusion, these findings highlight the rapid oxidation process of Eu that occurs without protective measures. To keep Eu in a metallic state, effective protection is required. Utilizing 2D materials such as hBN is effective in protecting metals such as Fe [14] or Eu, as evidenced in the latter case by the formation of Eu-Pt ferromagnetic compounds under the hBN layer on the Pt substrate [20]. Understanding how Eu behaves when intercalated beneath hBN is crucial to maximizing its potential in practical applications.

4. Eu/hBN/Ir(111) interface

The Eu deposition was carried out at low rates of approx. 0.001 Å/s as previously measured by quartz microbalance at the deposition position. Mostly, Eu was evaporated on the sample for 15 min, with the sample held at the indicated temperatures. The pressure during evaporation was $3 \cdot 10^{-9}$ mbar or better. The Eu coverage given throughout the manuscript is based on the intensity decrease of the Ir 4f core level from XPS analysis. A detailed description is included together with Fig. S6 in SM [47]. Shortly, for hBN growth and for a small Eu amount at the interface, the intensity of the substrate Ir 4f emission decreases due to the short electron mean free path of the outgoing photoelectrons. This reduction can be used for complete layers and for the small coverage cases, where Eu is localized just in the layer below hBN. For higher coverage, however, when Eu partially dissolves inside the Ir, this method does not work reliably anymore, but there the evaporation time and additionally the Eu 3d XPS intensity is used as a measure of Eu coverage. The coverage calibration can be corroborated by the di-valent Eu 3d emission in XPS that saturates when the maximum surface coverage is achieved (1/3 ML for the $(\sqrt{3} \times \sqrt{3})$R30° superstructure). If Eu is deposited beyond this amount, it diffuses into the bulk of the Ir substrate or may remain atop the hBN layer. In the first case scenario, the additional Eu atoms exhibit a tri-valent state (Eu^{3+}), which does not affect the ordered LEED pattern arising from the interface. For the second scenario, the excess Eu on top of hBN would be initially di-valent Eu but would quickly oxidizes to tri-valent Eu that can be easily detected by XPS analysis. This second scenario was not detected for high substrate temperatures as the ones used here, but only for quite low intercalation temperatures and very large Eu coverage that saturates the Ir near-surface region by the diffused Eu atoms.

A thorough study utilizing LEED was performed both before and after the intercalation of Eu to examine the structural characteristics in detail. Table 1 presents substrate temperature, actual Eu coverage on the sample surface, superstructure and the surface composition. The LEED pattern of the pristine Ir(111) surface is displayed in Fig. 2(a), where a red line connects two of the identical 3-fold Ir spots. Upon hBN growth at a temperature of 1220 K, a distinctive Moiré pattern emerges, characterized by a (12 × 12) hBN unit cell that occupies (11 × 11) Ir atoms. This is consistent with the observations made by Farwick et al. [51], as highlighted in Fig. 2(b). The blue line connecting the most intense spots is characteristic of the hBN unit cell in reciprocal space. Next, we investigated the effects of different intercalation conditions after the Eu deposition process through experiments conducted at various substrate temperatures, as depicted in Figs. 2(c)–(e). Temperature variations significantly alter the interface structure, leading to varying coverage. This observation aligns with the findings by Bakhit et al. [20]

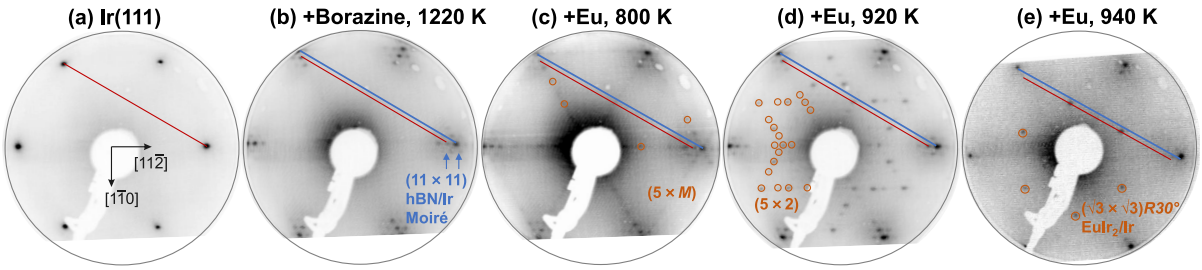

Fig. 2. Low energy electron diffraction (LEED) analysis of the experiment. (a) clean Ir(111), (b) after exposure to borazine at T_{Sample} = 1220 K, a Moiré pattern appears, consisting of a (12 × 12) hBN unit cell on (11 × 11) Ir atoms. Eu intercalation was carried out at different temperatures on freshly prepared hBN/Ir(111): (c) for 0.12 ML Eu at T_{Sample} = 800 K, a (5 × M) superstructure forms, where M > 2; (d) 0.9 ML Eu at T_{Sample} = 920 K, a (5 × 2) superstructure is observed; and (e) 0.3 ML Eu at T_{Sample} = 940 K, a $(\sqrt{3} \times \sqrt{3})R30°$ superstructure is seen. LEED images were captured at a kinetic energy of 60 eV. The lines in part of the patterns serve as a guide to the eye to distinguish the spots and enable assignment to the Ir substrate or hBN lattice.

Table 1
Experimental parameters of Eu intercalation below hBN on an Ir(111) substrate are presented, including various deposition temperatures, actual Eu coverage on the sample surface, superstructures formed after the Eu intercalation and surface composition Eu: Ir.

Deposition temperatures (K)	Actual Eu coverage on the sample surface (ML)	Superstructure	Surface composition Eu:Ir
800	0.12	(5 × M)	unknown
920	0.9	(5 × 2)	3:7
940	0.3	$(\sqrt{3} \times \sqrt{3})$R30°	1:2

and Schumacher et al. [28]. They emphasize the substantial influence of thermal factors and Eu coverage on the process of Eu intercalation.

At low Eu coverage of about 0.12 ML and substrate temperature 800 K, a (5 × M) superstructure was observed by LEED with respect to the Ir(111) substrate, see Fig. 2(c). A coincidence lattice appears exclusively along the <11$\bar{2}$> directions; however, achieving uniform alignment along the <$\bar{1}$10> directions is detained at low coverage, resulting in blurred LEED spots due to disorder. The parameter M, indicating periodicity along the <$\bar{1}$10> directions, suggests a random distribution of Eu atoms, occupying spaces between every 2 to 5 Ir atoms. This irregularity results in line like features and in less defined hBN/Ir Moiré spots along the <$\bar{1}$10> directions, although the overall Moiré pattern remains unchanged due to the fact that it arises mainly from non-intercalated hBN/Ir areas. This was concluded from the STM analysis shown in Fig. 4(b), (d) and (e). Further exposure of the (Eu)/hBN/Ir system to Eu at 920 K led to a compression of the intercalated layer, forming a (5 × 2) superstructure in three rotational domains, as depicted in Fig. 2(d). In this case, 0.9 ML Eu was deposited in total. This compression is attributed to an increased presence of Eu atoms along the <$\bar{1}$10> directions. The higher amount of Eu no longer allows for random occupation of Ir rows but instead positions every two Ir rows, indicating a stable superstructure relative to the Ir substrate. In the SM [47], Fig. S7 presents the LEED patterns of the (5 × 2) superstructure with variation in the kinetic energy of the electron.

In a different preparation, Eu was deposited on hBN/Ir(111) holding the substrate at 940 K but this time slowly evaporating a critical amount of Eu (30 min) to leave the Eu atoms just occupying surface positions and arrange in a $(\sqrt{3} \times \sqrt{3})R30°$ superstructure as presented in Fig. 2(e). At this coverage, a 2D surface phase $EuIr_2$ alloy is formed with a stoichiometry of one Eu atom per two Ir atoms, although the calculated amount from the decrease of the Ir 4f level resulted in 0.3 ML coverage. Previous studies have demonstrated the appearance of such superstructures as an indication of the formation of rare earth-gold and rare earth-silver surface alloys with a similar one-to-two ratio [52–58]. Moreover, the same superstructure was identified in a prior investigation of the Eu-Pt system [20]. Note that the Eu spots are associated with the Ir substrate, not with the hBN overlayer, which would produce superstructure spots on the blue line connecting hBN spots. This situation is partially distinct from the Eu intercalation below graphene on Ir(111) [28].

The saturation coverage is one-third ML of Eu, leading to the formation of a $(\sqrt{3} \times \sqrt{3})R30°$ superstructure with stoichiometry of one Eu atom per two Ir atoms displayed in Figs. 3(a) and (b), show its reciprocal lattice, while (c) presents the corresponding real-space structure. At 0.9 ML Eu coverage, a (5 × 2) superstructure appears, as seen in Fig. 3(d). This is evident in the STM analysis, further discussed in the text. The complexity of this superstructure is attributed to rotational domains, illustrated in Fig. 3(e) by the reciprocal lattice of the (5 × 2) superstructure with three rotational domains at 120° angle, alongside the Ir reciprocal lattice in gray. Here, it is important to say that only the lattice is considered, not a possible basis inside the lattice is discussed. Such a basis would not change the diffraction pattern, but eventually the composition. Later, it will be shown by STM that there are 3 Eu atoms present in each (5 × 2) unit. The alignment between the theoretical model and the LEED pattern is obvious. Finally, Fig. 3(f) illustrates the real-space structure of the (5 × 2) superstructure, highlighting both the Ir and Eu-Ir unit cells. Again, we will analyze next in the microscopy part that in reality we have 3 Eu atoms per unit cell, i.e., apart from the lattice. Then, inside of the 10 atoms in that (5 × 2) structure, three Eu atoms will give rise to a 0.3 ML Eu coverage.

The crystal structure of bulk $EuIr_2$ is a Laves phase $MgCu_2$ type structure according to reports in the literature [59]. The lattice parameter of this structure is 7.565 nm [60], indicating a stable [61] and well-defined crystallographic arrangement. In such a scenario, it is likely that Eu has di-valent character on the surface but tri-valent behavior in the bulk. This, together with eventual oxidation to EuO, gave rise to the initial confusion of a supposed di-valent valence state of the Eu atoms within bulk $EuIr_2$ due to magnetic measurements [62]. Di-valent surface but tri-valent bulk valence, on the other hand side, is quite often encountered for Eu-Ni or Eu-Pd systems [63,64].

STM images in Fig. 4 provide detailed insights into the hBN/Ir(111) Moiré pattern and the effects of Eu intercalation on its topography.

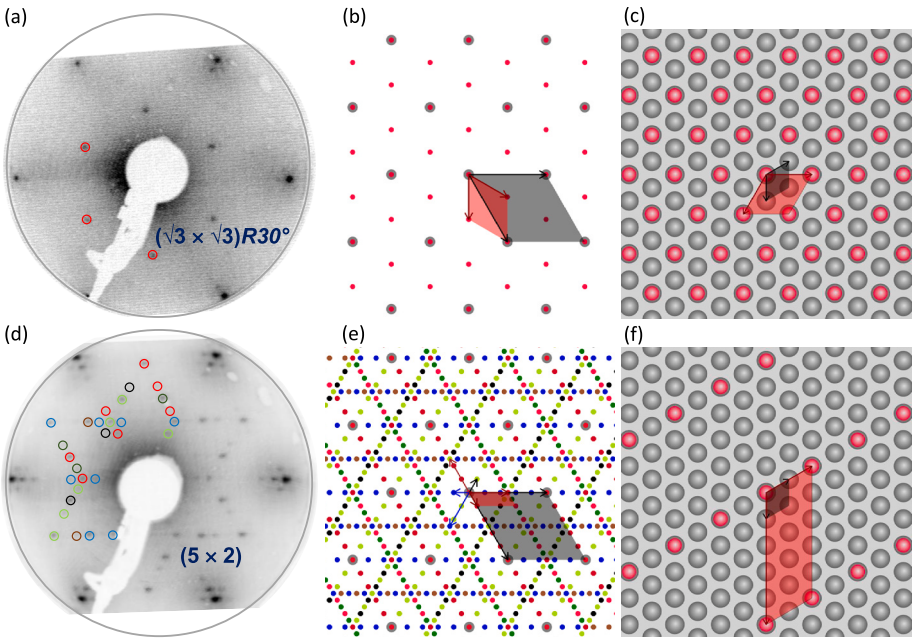

Fig. 3. (a) LEED image taken after high-temperature Eu intercalation of 0.3 ML at 940 K that reveals a $(\sqrt{3} \times \sqrt{3})R30°$ superstructure, (b) the reciprocal lattice, and (c) the structural model in real space. For the lower temperature (920 K) Eu intercalation, (d) presents the LEED image of the (5 × 2) superstructure that corresponds to a superposition of three rotational domains (e) with one of the (5 × 2) reciprocal unit cells in red and the Ir lattice in gray. (f) Structural model of the (5 × 2) superstructure in real space. LEED images in (a) and (d) were taken at electron beam energies of 60 eV and 55 eV, respectively.

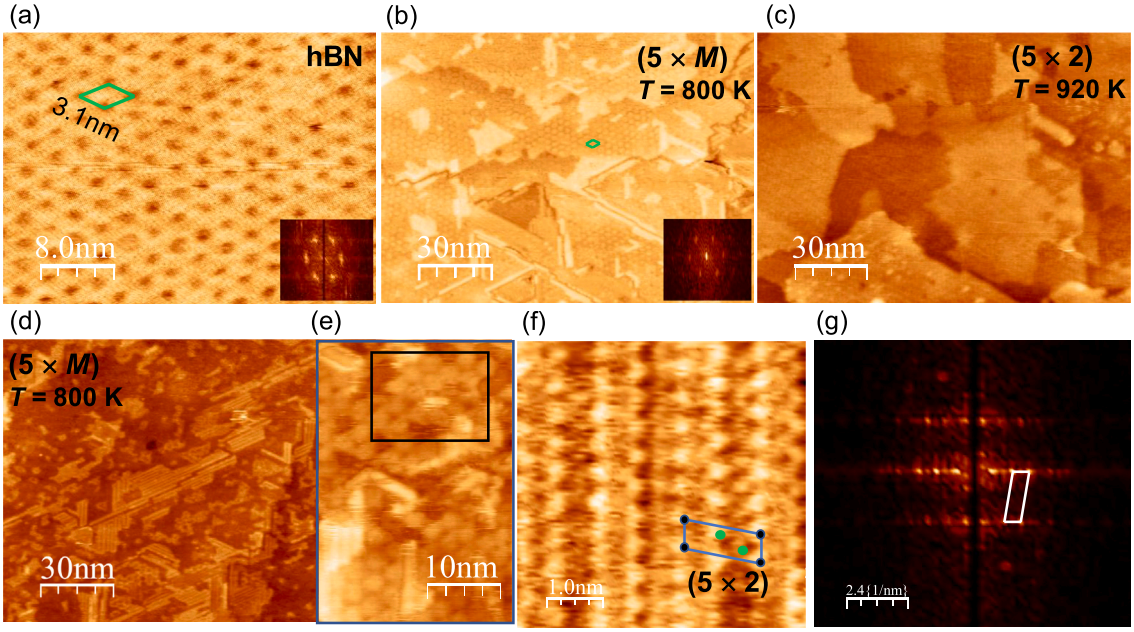

Fig. 4. (a) STM image of hBN/Ir(111) Moiré, the green hexagon represents the Moiré lattice with lattice parameter (3.1 ± 0.1)nm and the inset shows an FT image containing a hexagonal pattern, corresponding to the hBN/Ir(111) Moiré. (b) After intercalation of 0.12 ML of Eu, the green hexagon shows the hBN/Ir(111) Moiré lattice, and the inset shows an FT image containing a hexagonal pattern, corresponding to the hBN/Ir(111) Moiré. (c) After depositing more than 0.3 ML of Eu, namely 0.9 ML. (d) and (e) STM images of 0.12 ML of Eu taken at different regions; the highlighted area in black in (e) shows Eu-free hBN/Ir(111) Moiré. (f) Zoom in on one of the stripes parts in (d), showing the atomic resolution of (5 × 2) superstructure in blue together with a basis in green and black dots (g) FT image of (f). Tunneling parameters: (a) I=0.13 nA; U_{bias}=1 V, (b) I=0.13 nA; U_{bias} = 0.7 V, (c) I=0.13 nA; U_{bias} = 1.0 V, (d) I=0.13 nA; U_{bias} = 1.1 V, (e) I=0.13 nA; U_{bias} = 0.3 V, (f) I=0.13 nA; U_{bias} = 0.3 V.

The distinctive Moiré unit cell, highlighted in green, is characterized by bright protrusions interspersed with slight central indentations. It has a lattice constant of (3.1 ± 0.1) nm, as confirmed by Fourier-transformed (FT) image analysis in the inset of Fig. 4(a), further supporting the findings from Farwick et al. [51]. However, the observed Moiré periodicity shows a slight deviation from the theoretical value of 3.25 nm predicted by the commensurate (13 × 13)/(12 × 12) hBN/Ir(111) superstructure model of Schulz et al. [65], which was established via DFT simulations. This deviation is attributed to localized geometric variations within the hBN overlayer, consistent with the present observations.

In the case of Eu intercalation beneath graphene on Ir(111) reported by Schumacher et al. [28], wrinkles and defects act as Eu intercalation

pathways. Photoemission microscopy revealed that Eu is mostly intercalated at the vicinity of wrinkles via nanoscale cracks. In particular, pentagon–heptagon defects in the grown graphene layer on Ir(111) were discussed, which possess a small out-of-plane deformation to enable Eu trapping and, in turn, allow Eu to travel below the graphene layer. Similar mechanisms for other guest atoms are suggested [66] if the interaction with the 2D layer is not so strong, e.g., gold atom intercalation mechanisms that occur at packers as investigated by Daukiya et al. [67]. While wrinkles were not observed for hBN on Ir(111) [68], grain boundary defects in the hBN monolayer investigated by Gibb et al. [69] are suggested as intercalation pathways together with structural defects for Eu in the Eu/hBN/Ir(111) system. Although there is no direct experimental evidence, this interpretation remains speculative. However, possibly similar intercalation pathways as in the case of Cs intercalation below hBN on Ir(111) reported by [70] are suggested.

Soon after the deposition of 0.12 ML of Eu, the atoms pass through intercalation pathways, forming patterns of stripes and islands, as seen in Fig. 4(b), where the brighter regions indicate intercalated areas. At low coverage, only 30% of the hBN layer is affected by Eu intercalation. Consequently, the hBN/Ir Moiré lattice remains observable, highlighted in green in Fig. 4(b), with the same Moiré lattice constant as observed in panel (a). However, slight deviations in the Moiré lattice constant are noted, which can be attributed to local strain induced by Eu intercalation. These manifest as small variations in the Moiré periodicity, slight distortions of the Moiré unit cell, and a minor reduction in long-range order due to locally modified hBN–substrate registry. The FT image is shown in the inset of Fig. 4(b). Variations in the distribution of intercalated Eu result in uneven concentrations, particularly in areas where dense stripes are visible, as displayed in Fig. 4(d). The Moiré pattern varies slightly depending on the density of the stripes, as shown in Figs. 4(b), (d), and (e) corresponding to different areas on the sample. Upon closer inspection of one of these stripes in Fig. 4(d), a locally formed (5×2) superstructure was observed. This superstructure was undetected in the LEED pattern, but is evident in Fig. 4(f), where the blue lattice together with black and green dots (Eu atoms) represents the (5×2) unit cell. The FT of a single domain of the (5×2) superstructure is shown in Fig. 4(g). However, a more uniform distribution of Eu intercalation is achieved below hBN when increasing the Eu coverage up to 0.9 ML, resulting in Fig. 4(c).

Core-level PE spectroscopy was utilized to examine the Eu intercalated layer beneath hBN on the Ir(111) substrate before and after intercalation, in order to understand its chemical composition and morphology. Investigating the impact of various Eu coverages on the chemical state of the system is of particular interest, as the Eu coverage is determined from the XPS spectra, as explained in the SM [47].

Before addressing the electronic properties of the Eu, the interdiffusion of Eu into Ir and the Eu-Ir alloy formation below the hBN layer will be addressed. Already in Fig. 1 it was shown that Eu diffuses into Ir in the absence of a hBN layer. This is also presented in SM [47] in Fig. S3, where the XPS survey for Eu/Ir preparation reveals a strong decrease of Ir core-level emissions, particularly the 4f core-level peaks, which indicates that the overlayer of Eu atoms has attenuated substrate photoemission. As the Eu coverage increases, the Ir signal becomes more and more obscured, which is consistent with this attenuation.

Now, in Fig. 5, the XPS survey spectra as well as the Ir $4f_{7/2}$ and Eu 3d are shown for two Eu coverages when hBN is present; the complete coverage series is shown in Fig. S8. In the survey spectra in Fig. 5(a), all relevant transitions of the system are indicated. The offset of these spectra is presented in Fig. S9 in the SM [47]. The main contributions arising from the Ir are the $4f_{7/2}$ of the 4f doublet, and for Eu, the 3d emission. Both regions are further indicated in parts (b) and (c) of Fig. 5. The low Eu coverage emission of 0.3 ML Eu (corresponding to a T = 940 K preparation with $(\sqrt{3} \times \sqrt{3})R30°$ LEED, see Fig. 2(e)) reveals Eu atoms in a di-valent configuration, i.e., below hBN but at the interface. This is reflected in the spectrum by the $3d_{5/2}$ and $3d_{3/2}$ emissions at −1123 eV and −1154 eV, respectively and the corresponding satellite emissions. On the other hand, the high Eu coverage spectra (0.9 ML) contain Eu in di-valent and tri-valent configurations. The di-valent emission is nearly identical to the 0.3 ML case, verifying the nearly complete coverage of Eu at the interface in both indicated cases. The excess Eu, however, diffuses into the Ir bulk, becoming tri-valent as in $EuIr_2$ compound [37]. Its energy position at −1133.4 eV is also different to the oxidized Eu^{3+} emission in Eu_2O_3 at −1135 eV [48], see also Fig. S11 in the SM [47]. For the Eu 3d emission, a relatively short electron mean free path of the electrons [73] of less than 1 nm and the equal intensity of both 2+ and 3+ components together with the knowledge of the deposited amount indicate that Eu distributes at several layers below the interface. The Eu atoms around Ir affect the energy of the Ir 4f emission as shown in Fig. 5(b). Note that the photoelectrons for the latter Ir 4f emission are more bulk sensitive due to a larger kinetic energy of the photoelectrons. Nevertheless, even with such a high kinetic energy, the surface component emission of Ir(111) may still influence the core level spectra. To depress at least partially the surface emission, the CO-saturated Ir(111) surface at 0.25 ML CO coverage was considered. This CO/Ir system lowers the Ir 4f surface emission to less than one half [74]. The Ir 4f emissions of the CO/Ir and the Ir with small Eu coverage below hBN reveal identical core level positions of the Ir $4f_{7/2}$, i.e., (i) mainly the Ir 4f sub-interface atoms have a strong weight on the photoemission peak and (ii) a possible interaction of Eu and Ir at the surface is not affecting the Ir "bulk" emission. Furthermore, room temperature deposition of Eu onto Ir results in the same Ir 4f core level energies (not shown). The Ir 4f spectrum of the high Eu coverage, however, has a small core level shift to higher binding energies at the Ir $4f_{7/2}$ line of (75 ± 20) meV. Such a small core level shift is expected in an Eu-Ir alloy since Eu is highly electropositive with respect to Ir, and electron transfer from Eu into the Ir d bands takes place. This situation is analogous to the $SmIr_2$ system, which has a similar core level shift [75]. This shift does not automatically mean that Ir atoms surrounded by Eu have really such a core level energy, but here we treat a sum of Ir emissions with and without Eu atoms. This increases the peak width, and all contributions sum to the mentioned core level shift. To summarize, the diffusion of Eu into Ir gives rise to the Eu-Ir alloy formation below the interface with a positive Ir 4f core level shift. Still, the interface itself was not yet considered. For this purpose, the Eu 3d emission will be analyzed. If a 2D surface phase alloy would be formed, one would expect a core level shift of the Eu emission in the contrary direction to that of the Ir 4f levels. Fig. 5(d) compares the di-valent part of the Eu $3d_{5/2}$ interface emission of the higher coverage (0.9 ML Eu/hBN) preparation with a sample that consists of approx. 0.5 ML Eu directly evaporated at room temperature onto clean Ir(111). In that latter case, due to the reduced temperature, Eu just stays at the surface but does not yet alloy with Ir. The broad di-valent Eu $3d_{5/2}$ emission is fit with two components (P1, P2) according to the peak fit approach in EuS [76]. The fit reveals a core-level shift of the intercalated Eu below hBN in the expected direction as a result of the surface alloying process by (−350 ± 50) meV. This means that alloying also takes place at the interface and is a temperature-induced process.

Next, we will address the electronic properties of 0.3 ML Eu intercalation at 940 K. Similar to it a very low coverage of 0.12 ML and lower intercalation temperature corresponding to 800 K, an identical shape of the Eu 3d spectrum is obtained, but only smaller in intensity (illustrated in SM [47], in Figs. S6 and S10).

The Eu 3d spectrum only displays a Eu^{2+} configuration with a shake-up peak observed at a higher binding energy, and no Eu^{3+} contribution is detected. Furthermore, the O 1s spectrum reveals no additional components compared to the pre-intercalation spectra, suggesting no oxygen presence, see Fig. S10.

With a further increase to 0.3 ML, the Eu 3d spectrum still displayed Eu in a di-valent state shown in Fig. 6. The existence of Eu^{2+} suggests that Eu stays at the interface. The $Eu^{2+}_{Sat.}$ satellite emissions (at −1132.6

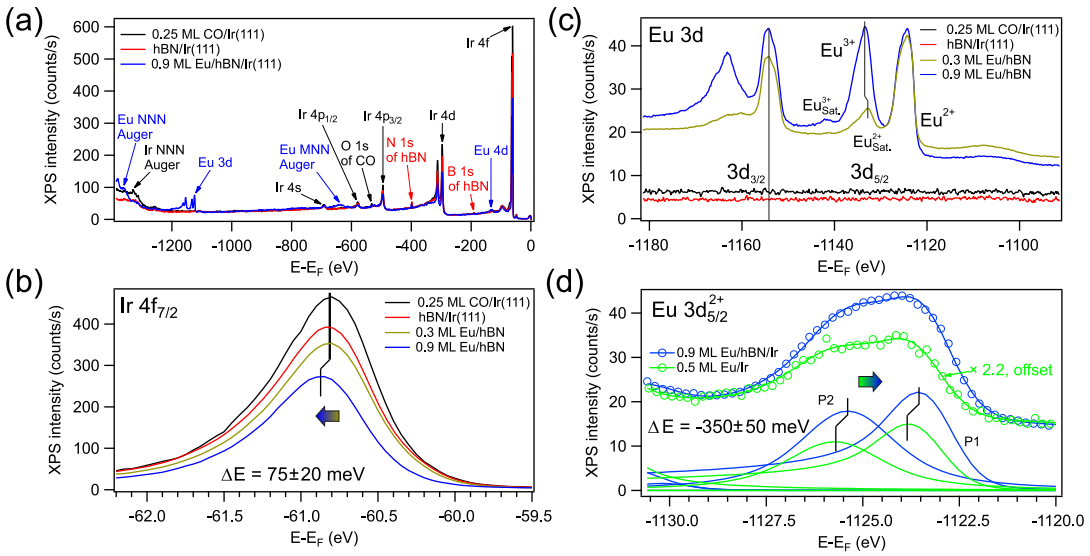

Fig. 5. XPS spectra for several preparations of Eu intercalated below hBN/Ir(111). (a) Survey spectra of the CO saturated Ir(111) surface, 1 ML hBN on clean Ir(111), and 0.9 ML Eu intercalated below hBN. Indicated are the observed transitions in the systems. (b), (c) Ir $4f_{7/2}$ and Eu 3d core level emissions of the spectra of (a) and additionally the 0.3 ML coverage preparation of the $(\sqrt{3}\times\sqrt{3})$R30° superstructure. (d) Eu^{2+} $3d_{5/2}$ core level region of the intercalated 0.9 ML Eu/hBN and the 0.5 ML Eu/Ir systems, the latter deposited at RT. The emissions were fit by a doublet of Doniach-Sunjic line shapes [71] on a Shirley background [72] to obtain the core level shift. ($h\nu$ = 1486.6 eV, Al K_α).

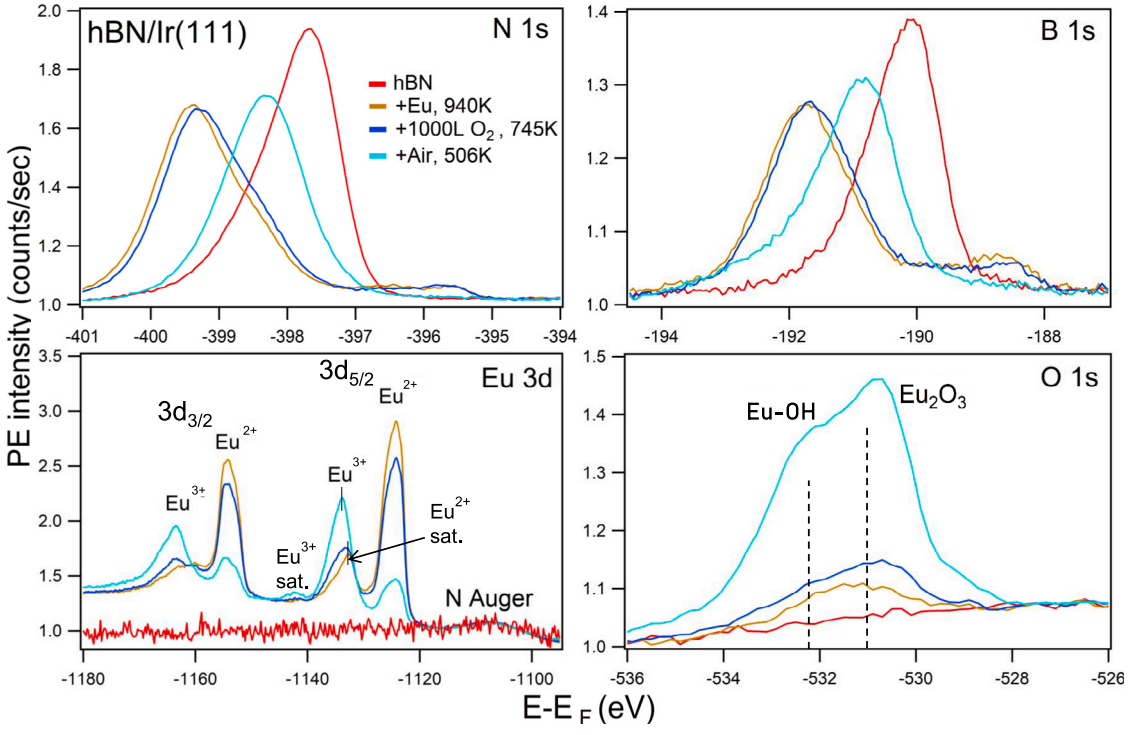

Fig. 6. XPS analysis of 0.3 ML Eu intercalation below hBN on Ir(111) crystal for an initial T = 940 K preparation corresponding to a $(\sqrt{3}\times\sqrt{3})$R30° superstructure. The core level spectra of N 1s, B 1s, Eu 3d, and O 1s X-ray photoemission spectra taken at $h\nu$ = 1486.6 eV (Al Kα) before and after exposure to 1000 L of oxygen are shown, additionally to the exposure to ambient conditions.

eV for the $3d_{5/2}$ peak) amounts to 18% of the leading Eu^{2+} [77–79]. Before Eu intercalation, the N 1s and B 1s spectra in Fig. 6 exhibited a distinct asymmetric peak shape, containing two components [1] with a pronounced shoulder at higher binding energies [51,80,81]. The strength of the substrate–overlayer interaction in this system is between the weak hBN on the Pt(111) and the intermediate hBN on the Rh(111) systems [82]. The same hBN quality was obtained in the second preparation acquired at a temperature of 1120 K.

After Eu intercalation, see Fig. 6, the N 1s and B 1s spectra exhibit a noticeable broadening and a shift of around 1.7 eV and 1.65 eV, respectively, towards higher binding energies. The observed shift originates from the electrostatic potential created by the ionized 2D surface phase $EuIr_2$ alloy formed at the interface. Acting as a capacitor-like layer between the substrate and hBN, this interfacial alloy induces an electrostatic potential that leads to a rigid displacement of the hBN electronic structure, as evidenced by the nearly identical shifts

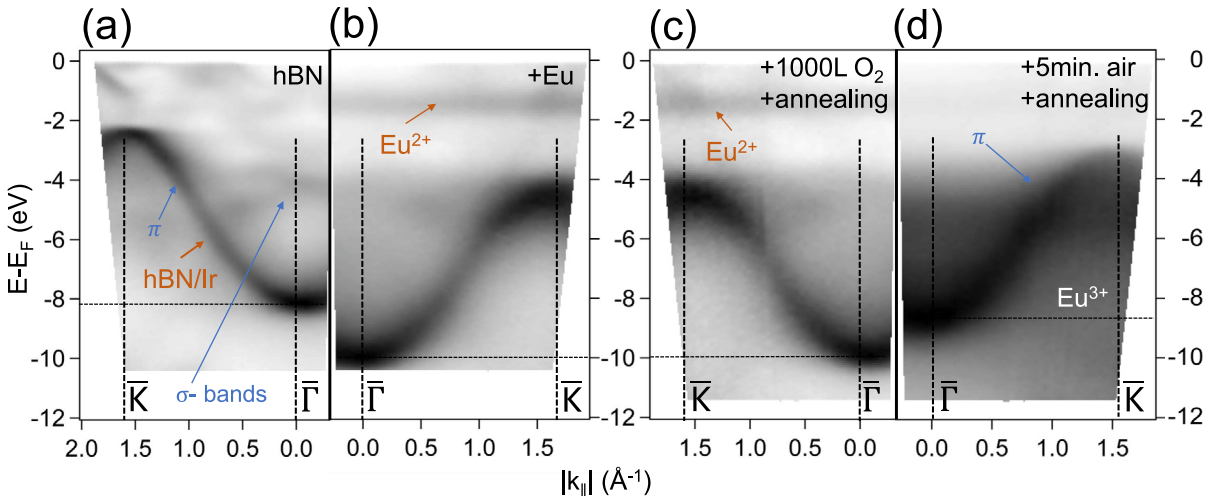

Fig. 7. ARPES analysis of the band structure of the hBN layer prior to and after Eu intercalation. He II α ($h\nu$ = 40.8 eV) photoemission intensity maps along [$\bar{\Gamma}$][$\bar{K}$] direction of the hBN band structure for (a) hBN/Ir(111), (b) after intercalation of 0.3 ML of Eu at T = 940 K, (c) after dosing 1000 L of O_2 and annealing T = 745 K, and (d) followed by air exposure and annealing at T = 506 K. The strongly dispersive band feature corresponds to the π-band of hBN at the indicated interfaces.

in the B 1s and N 1s core levels. Similar behavior was reported by Fedorov et al. [83] where substrate functionalization induces interfacial charge rearrangement and dipole formation, generating an electrostatic potential that shifts the hBN electronic structure. This led to a stronger interaction between the hBN layer and the 2D surface phase $EuIr_2$ alloy, which alters the local electrostatic environment and leads to enhanced interfacial coupling compared to the pristine hBN/Ir(111) system. Our results also confirm the findings of Cs adsorption and intercalation at hBN/Ir(111) [70]. Furthermore, a side peak detected at lower binding energies was interpreted to originate from single B and N atoms, consistent with the findings reported by [80]. In this preparation here, due to the long deposition time and high temperature, a small part of Eu got oxidized. Taking into account the Eu 3d and O 1s cross sections [84], approx. 7% of Eu got oxidized during deposition and sample handling. Upon exposure to 1000 L of O_2, a slight shift towards lower binding energies was detected in the N and B 1s spectra. However, these spectra retained the same characteristics as those inspected prior to exposure. The Eu 3d spectrum shows a notable decrease in Eu^{2+} with a simultaneous increase in Eu^{3+} aside the Eu^{2+} satellite peak, indicating the formation of oxides and hydroxides. This situation is confirmed by the increase in O 1s spectrum that now reveals a double-peak structure corresponding to Eu_2O_3 and Eu-OH at E-E_F= −532.3 eV and −531.0 eV, respectively. In addition, a small EuO component at E-E_F= −529.6 eV was determined from the fitting results of the O 1s spectra after Eu intercalation, as shown in the SM [47] in Fig. S11. Here, the observation can be compared to the pure Eu deposition and successive oxidation shown in Fig. 1. There with a accumulated dosage of 1.5 L of rest gas, the Eu got nearly completely oxidized while here, below hBN, only a small amount is affected after 1000 L O_2 dosage.

Subsequently, the system was exposed to ambient conditions followed by vacuum annealing at 506 K to remove some impurities. As a result, the N 1s and B 1s spectra began to recover their initial shape and position, indicating that the contact interface changed from a strong interaction with the 2D surface phase $EuIr_2$ alloy to a weaker interaction with Eu_2O_3. Similar trends were noted in related systems, as reported in recent research [20]. The overall intensity of the Eu 3d spectra in Fig. 5 decreases significantly. It shows a doubling of the Eu^{3+} amount, accompanied by a substantial reduction in the Eu^{2+} amount. Moreover, the O 1s spectrum shows a remarkable increase in both Eu_2O_3 and Eu-OH components and a decrease in the EuO component. The fit presented in the SM [47], in Fig. S11, reveals a further component with an E-E_F= −533.0 eV corresponding to adsorbed water. The di-valent Eu component now has approx. 20% of its initial value, i.e., this constitutes the protected part after air exposure without yet taking into account the photoelectron damping due to additional contaminations on top of the hBN layer. Note that oxidation takes place preferentially at defect sites, leading to partial oxidation of the intercalated Eu. However, this resulting oxidized species appear to provide a form of protection to that small protected amount. This also highlights that the effectiveness of hBN as a protective layer is limited.

Lastly, let us comprehensively address the electronic band structure of the (Eu)/hBN/Ir(111) system before and after air exposure. This was investigated using ARPES with He IIα light at photon energy $h\nu$ = 40.8 eV, as shown in Fig. 7. This photon energy is very suitable for the emission of the hBN π band but less suitable for the σ bands. The study focuses in particular on the impact of air exposure on the hBN-protecting layer. In Fig. 7, the hBN π band disperses from its minimum energy at $\bar{\Gamma}$ upwards towards the $\bar{K}$ point where it reaches the closest energy to the Fermi level, representing the minimum and maximum energy of the surface Brillouin zone. This band extends from −8.0 to −2.4 eV upon hBN growth, while the Ir valence bands lie noticeably closer to the Fermi level. After intercalating one-third ML of Eu, the hBN π band shifts by 2 eV to higher binding energies, and the di-valent Eu 4f emissions appear as a flat band at approx. 1.6 eV binding energy. The π-band shift results due to the strong interaction of the hBN with the 2D surface phase $EuIr_2$ alloy interface; such π band shifts were observed in other systems [29,70,83,85–89]. Upon exposure to 1000 L of oxygen, the π band of the hBN exhibited a slight shift, while the di-valent Eu 4f intensity is maintained corroborating our XPS results. However, all bands became somewhat blurred after air exposure. Despite this, the hBN π band is still observed, with a notable shift towards lower binding energies, i.e., a partial recovery of the hBN π band. The di-valent Eu 4f emission is nearly invisible, but the tri-valent Eu 4f emission appears between −4 and −10 eV. Thus, neither oxygen nor air exposure affects the hBN layer itself.

5. Conclusion

We examined the structural and electronic properties of Eu intercalated beneath hBN on an Ir(111) substrate at various deposited Eu amounts and temperatures. The analysis using LEED indicated the presence of distinct superstructures, specifically (5 × M), (5 × 2) and ($\sqrt{3} \times \sqrt{3}$)$R30°$ depending mainly on preparation temperature. The (5 × M) superstructure, resulting from 0.12 ML deposited Eu amount, exhibits a unidirectional ordering of Eu atoms due to the low amount.

It is a precursor of the (5 × 2) phase with 3 Eu atoms in the unit cell obtained at higher coverage and T = 920 K. Finally, at 940 K, a $(\sqrt{3} \times \sqrt{3})R30°$ structure emerges corresponds to 0.3 ML Eu coverage in a 2D surface phase $EuIr_2$ alloy. In all cases, the Eu is below the hBN layer with the interface atoms in a di-valent configuration, but the excess Eu atoms that diffuse into the Ir bulk have a 3+ configuration. The STM observations of Eu intercalation and the resulting structural modifications are consistent with the XPS findings, which reveal changes in the chemical environment through the N 1s and B 1s core-level shifts. Moreover, these chemical changes are reflected in the ARPES results as modifications in the electronic band structure, such as the shift of the hBN π band due to stronger interaction with the formed 2D surface phase $EuIr_2$ alloy and the evolution of Eu 4f states. This combination of experimental findings provides a comprehensive understanding of the Eu intercalation below hBN on Ir(111) system. Lastly, Eu below the hBN layer is at least 20% protected from oxidation, even after air exposure, quite in contrast to an unprotected Eu-Ir surface alloy that already presents degradation under UHV conditions.

CRediT authorship contribution statement

Alaa Mohammed Idris Bakhit: Writing – review & editing, Writing – original draft, Visualization, Validation, Methodology, Investigation, Funding acquisition, Formal analysis, Conceptualization. **Khadiza Ali:** Writing – review & editing, Investigation, Data curation. **Anna A. Makarova:** Data curation, Resources. **Frederik Schiller:** Writing – review & editing, Supervision, Resources, Project administration, Methodology, Funding acquisition, Data curation, Conceptualization.

Declaration of competing interest

The authors declare the following financial interests/personal relationships which may be considered as potential competing interests: Frederik Schiller reports financial support was provided by Spain Ministry of Science and Innovation. Frederik Schiller reports financial support was provided by Basque Government. Frederik Schiller reports financial support was provided by Gipuzkoa Next program of the Diputación Foral de Gipuzkoa. Frederik Schiller reports financial support was provided by the EU Horizon 2020 Framework Programme for Research and Innovation. Alaa Mohammed Idris Bakhit reports financial support was provided by Fomento San Sebastián. Alaa Mohammed Idris Bakhit reports financial support was provided by European Network for Innovative and Advanced Epitaxy. If there are other authors, they declare that they have no known competing financial interests or personal relationships that could have appeared to influence the work reported in this paper.

Acknowledgments

We acknowledge the financial support received from the Spanish MCIN/AEI/10.13039/501100011033 through grant PID2023-149158OB-C44, as well as the Basque Government, Spain through the grant IT-1591-22 and Gipuzkoa Next program of the Diputación Foral de Gipuzkoa, Spain DFG- 2023-CIEN-000077. We also express our gratitude to Fomento San Sebastián and COST-action OPERA for their funding contributions. We acknowledge the Helmholtz-Zentrum Berlin für Materialien und Energie Facility for the allocation of beam time on the GELEM Dipole. The access was provided through Proposal 232-12274-ST.

Appendix A. Supplementary data

Supplementary material related to this article can be found online at https://doi.org/10.1016/j.apsusc.2026.167568.

Data availability

Data will be made available on request.

References

[1] A. Preobrajenski, M. Nesterov, M.L. Ng, A. Vinogradov, N.M. artensson, Monolayer h-BN on lattice-mismatched metal surfaces: On the formation of the nanomesh, Chem. Phys. Lett. 446 (1) (2007) 119–123, http://dx.doi.org/10.1016/j.cplett.2007.08.028.
[2] W. Auwärter, Hexagonal boron nitride monolayers on metal supports: Versatile templates for atoms, molecules and nanostructures, Surf. Sci. Rep. 74 (1) (2019) 1–95, http://dx.doi.org/10.1016/j.surfrep.2018.10.001.
[3] I. Demiroglu, F.M. Peeters, O. Gülseren, D. Çakır, C. Sevik, Alkali Metal Intercalation in MXene/Graphene Heterostructures: A New Platform for Ion Battery Applications, J. Phys. Chem. Lett. 10 (4) (2019) 727–734, http://dx.doi.org/10.1021/acs.jpclett.8b03056.
[4] M. Pustilnik, K.A. Matveev, Solitons in a one-dimensional wigner crystal, Phys. Rev. B 91 (2015) 165416, http://dx.doi.org/10.1103/PhysRevB.91.165416.
[5] J. Coraux, A.T. N'Diaye, N. Rougemaille, C. Vo-Van, A. Kimouche, H.-X. Yang, M. Chshiev, N. Bendiab, O. Fruchart, a.K. Schmid, Air-Protected Epitaxial Graphene/Ferromagnet Hybrids Prepared by Chemical Vapor Deposition and Intercalation, J. Phys. Chem. Lett. 3 (15) (2012) 2059–2063, http://dx.doi.org/10.1021/jz3007222.
[6] M.-B. Martin, B. Dlubak, R.S. Weatherup, M. Piquemal-Banci, H. Yang, R. Blume, R. Schloegl, S. Collin, F. Petroff, S. Hofmann, J. Robertson, A. Anane, A. Fert, P. Seneor, Protecting nickel with graphene spin-filtering membranes: A single layer is enough, Appl. Phys. Lett. 107 (1) (2015) 012408, http://dx.doi.org/10.1063/1.4923401.
[7] R.S. Weatherup, L. D'Arsié, a. Cabrero-Vilatela, S. Caneva, R. Blume, J. Robertson, R. Schloegl, S. Hofmann, Long-Term Passivation of Strongly Interacting Metals with Single-Layer Graphene, JACS 137 (45) (2015) 14358–14366, http://dx.doi.org/10.1021/jacs.5b08729.
[8] M. Cattelan, G.W. Peng, E. Cavaliere, L. Artiglia, A. Barinov, L.T. Roling, M. Favaro, I. Píš, S. Nappini, E. Magnano, F. Bondino, L. Gavioli, S. Agnoli, M. Mavrikakis, G. Granozzi, The nature of the fe–graphene interface at the nanometer level, "Nanoscale" 7 (2015) 2450–2460, http://dx.doi.org/10.1039/C4NR04956J.
[9] H. Naganuma, V. Zatko, M. Galbiati, F. Godel, A. Sander, C. Carrétéro, O. Bezencenet, N. Reyren, M.-B. Martin, B. Dlubak, P. Seneor, A perpendicular graphene/ferromagnet electrode for spintronics, Appl. Phys. Lett. 116 (17) (2020) 173101, http://dx.doi.org/10.1063/1.5143567.
[10] P. Sutter, J.T. Sadowski, E.A. Sutter, Chemistry under Cover: Tuning Metal-Graphene Interaction by Reactive Intercalation, JACS 132 (23) (2010) 8175–8179, http://dx.doi.org/10.1021/ja102398n.
[11] I.S. Sokolov, D.V. Averyanov, O.E. Parfenov, I.A. Karateev, A.N. Taldenkov, a.M. Tokmachev, V.G. Storchak, 2D ferromagnetism in europium/graphene bilayers, "Mater. Horiz." 7 (2020) 1372–1378, http://dx.doi.org/10.1039/C9MH01988J.
[12] N.A. anderson, M. Hupalo, D. Keavney, M.C. Tringides, D. Vaknin, Intercalated europium metal in epitaxial graphene on SiC, Phys. Rev. Mater. 1 (2017) 054005, http://dx.doi.org/10.1103/PhysRevMaterials.1.054005.
[13] M. Liu, Y. Li, P. Chen, J. Sun, D. Ma, Q. Li, T. Gao, Y. Gao, Z. Cheng, X. Qiu, Y. Fang, Y. Zhang, Z. Liu, Quasi-freestanding monolayer heterostructure of graphene and hexagonal boron nitride on Ir(111) with a zigzag boundary, Nano Lett. 14 (11) (2014) 6342–6347, http://dx.doi.org/10.1021/nl502780u.
[14] S. Caneva, M.-B. Martin, L. D'Arsié, A.I. Aria, H. Sezen, M. Amati, L. Gregoratti, H. Sugime, S. Esconjauregui, J. Robertson, S. Hofmann, R.S. Weatherup, From Growth Surface to Device Interface: Preserving Metallic Fe under Monolayer Hexagonal Boron Nitride, ACS Appl. Mater. Interfaces 9 (35) (2017) 29973–29981, http://dx.doi.org/10.1021/acsami.7b08717.
[15] L. Jiang, N. Xiao, B. Wang, E. Grustan-Gutierrez, X. Jing, P. Babor, M. Kolíbal, G. Lu, T. Wu, H. Wang, et al., High-resolution characterization of hexagonal boron nitride coatings exposed to aqueous and air oxidative environments, Nano Res. 10 (2017) 2046–2055, http://dx.doi.org/10.1007/s12274-016-1393-2.
[16] X. Tang, H. Wang, C. Liu, X. Zhu, W. Gao, H. Yin, Direct Growth of Hexagonal Boron Nitride Nanofilms on Stainless Steel for Corrosion Protection, ACS Appl. Nano Mater. 4 (11) (2021) 12024–12033, http://dx.doi.org/10.1021/acsanm.1c02590.
[17] J. Holler, L. Bauriedl, T. Korn, a. Seitz, F. Özyigit, M. Eichinger, C. Schüller, K. Watanabe, T. Taniguchi, C. Strunk, N. Paradiso, Air tightness of hBN encapsulation and its impact on Raman spectroscopy of van der waals materials, 2D Mater., vol. 7 (1) (2019) 015012, http://dx.doi.org/10.1088/2053-1583/ab4723.
[18] S. Zihlmann, P. Makk, C.A.F. Vaz, C. Schönenberger, Role of hexagonal boron nitride in protecting ferromagnetic nanostructures from oxidation, in: 2D Mater., 3 (1) (2016) 011008, http://dx.doi.org/10.1088/2053-1583/3/1/011008.
[19] K.Y. Ma, L. Zhang, S. Jin, Y. Wang, S.I. Yoon, H. Hwang, J. Oh, D.S. Jeong, M. Wang, S. Chatterjee, et al., Epitaxial single-crystal hexagonal boron nitride multilayers on Ni(111), Nat. 606 (7912) (2022) 88–93, http://dx.doi.org/10.1038/s41586-022-04745-7.

[20] A. Mohammed Idris Bakhit, K. Ali, A.A. Makarova, I. Píš, F. Bondino, R. Sant, S.P. Dash, R. Castrillo-Bodero, Y. Hasegawa, J.E. Ortega, L. Fernandez, F. Schiller, A ferromagnetic Eu–Pt surface compound grown below hexagonal boron nitride, "Nanoscale" 15 (2023) 11517–11528, http://dx.doi.org/10.1039/D3NR00630A.

[21] E. Voloshina, F. Schiller, K. Ali, A. Mohammed Idris Bakhit, R. Castrillo-Bodero, B. Paulus, Y. Dedkov, Europium intercalation as a route to modulate electronic and magnetic properties of h-BN/Ni(111), "Nanoscale" (2025) http://dx.doi.org/10.1039/D5NR03875H.

[22] A. Ugale, T.N. Kalyani, S.J. Dhoble, 2 - potential of europium and samarium β-diketonates as red light emitters in organic light-emitting diodes, in: P.M. n Ramos, M. Ramos Silva (Eds.), Lanthanide-Based Multifunctional Materials, in: Advanced Nanomaterials, Elsevier, 2018, pp. 59–97, http://dx.doi.org/10.1016/B978-0-12-813840-3.00002-8.

[23] J.M. Lawrence, P.S. Riseborough, R.D. Parks, Valence fluctuation phenomena, Rep. Progr. Phys. 44 (1) (1981) 1, http://dx.doi.org/10.1088/0034-4885/44/1/001.

[24] Z. Hossain, C. Geibel, N. Senthilkumaran, M. Deppe, M. Baenitz, F. Schiller, S.L. Molodtsov, Antiferromagnetism, valence fluctuation, and heavy-fermion behavior in $EuCu_2(Ge_{1-x}Si_x)_2$, Phys. Rev. B 69 (2004) 014422, http://dx.doi.org/10.1103/PhysRevB.69.014422.

[25] K.S. Nemkovski, D.P. Kozlenko, P.A. Alekseev, J.-M. Mignot, A.P. Menushenkov, A.A. Yaroslavtsev, E.S. Clementyev, A.S. Ivanov, S. Rols, B. Klobes, R.P. Hermann, A.V. Gribanov, Europium mixed-valence, long-range magnetic order, and dynamic magnetic response in $EuCu_2(Si_xGe_{1-x})_2$, Phys. Rev. B 94 (2016) 195101, http://dx.doi.org/10.1103/PhysRevB.94.195101.

[26] M. Jugovac, I. Cojocariu, J. Sánchez-Barriga, P. Gargiani, M. Valvidares, V. Feyer, S. Blügel, G. Bihlmayer, P. Perna, Inducing single spin-polarized flat bands in monolayer graphene, Adv. Mater. 35 (38) (2023) 2301441, http://dx.doi.org/10.1002/adma.202301441.

[27] M. Jugovac, I. Cojocariu, G. Bihlmayer, P. Gargiani, M. Valvidares, C.A. Brondin, S. Blügel, A. Locatelli, T.O. Mentes, P. Perna, Persistent magnetism and tunable doping of monolayer graphene via europium density modulation, Adv. Sci. 13 (7) (2026) e21592, http://dx.doi.org/10.1002/advs.202521592.

[28] S. Schumacher, F. Huttmann, M. Petrović, C. Witt, D.F. Förster, C. Vo-Van, J. Coraux, A.J. Martínez-Galera, V. Sessi, I. Vergara, R. Rückamp, M. Grüninger, N. Schleheck, F. Meyer zu Heringdorf, P. Ohresser, M. Kralj, T.O. Wehling, T. Michely, Europium underneath graphene on Ir(111): Intercalation mechanism, magnetism, and band structure, Phys. Rev. B 90 (2014) 235437, http://dx.doi.org/10.1103/PhysRevB.90.235437.

[29] U.A. Schröder, M. Petrović, T. Gerber, A.J. Martínez-Galera, E. Gr° anäs, M.A. Arman, C. Herbig, J. Schnadt, M. Kralj, J. Knudsen, T. Michely, Core level shifts of intercalated graphene, 2D Mater., vol. 4 (1) (2016) 015013, http://dx.doi.org/10.1088/2053-1583/4/1/015013.

[30] I.S. Sokolov, D.V. Averyanov, O.E. Parfenov, A.N. Taldenkov, I.A. Karateev, A.M. Tokmachev, V.G. Storchak, Two-dimensional ferromagnetism in Eu-intercalated few-layer graphene, J. Alloys Compd. 884 (2021) 161078, http://dx.doi.org/10.1016/j.jallcom.2021.161078.

[31] P. Valerius, Low-energy ion irradiation and thermal annealing of supported 2D materials (Ph.D. thesis), Universität zu Köln, Germany, 2020, URL https://kups.ub.uni-koeln.de/11347/.

[32] A.M.I. Bakhit, Growth, and electronic properties of Rare-earth - noble metal Surface compounds grown on curved single crystals and its protection by 2D Materials (Ph.D. thesis), Univerity of the Basque Country UPV-EHU, Spain, 2025.

[33] R.M. Bozorth, B.T. Matthias, H. Suhl, E. Corenzwit, D.D. Davis, Magnetization of Compounds of Rare Earths with Platinum Metals, Phys. Rev. 115 (1959) 1595–1596, http://dx.doi.org/10.1103/PhysRev.115.1595.

[34] R.M. Bozorth, J.H. Van Vleck, Magnetic Susceptibility of Metallic Europium, Phys. Rev. 118 (1960) 1493–1498, http://dx.doi.org/10.1103/PhysRev.118.1493.

[35] B.T. Matthias, R.M. Bozorth, J.H. Van Vleck, Ferromagnetic interaction in EuO, Phys. Rev. Lett. 7 (1961) 160–161, http://dx.doi.org/10.1103/PhysRevLett.7.160.

[36] J. Van Vleck, How EuO was discovered, J. Less-Common Met. 62 (1978) xv–xvii, http://dx.doi.org/10.1016/0022-5088(78)90007-3.

[37] M. Peter, B.T. Matthias, Paramagnetic resonance in metallic europium and intermetallic compounds, Phys. Rev. Lett. 4 (1960) 449–450, http://dx.doi.org/10.1103/PhysRevLett.4.449.

[38] B.T. Matthias, Z. Fisk, J.L. Smith, Superconductivity with Europium, Phys. Lett. A 72 (3) (1979) 257–258, http://dx.doi.org/10.1016/0375-9601(79)90021-5.

[39] U. Stockert, S. Seiro, N. Caroca-Canales, E. Hassinger, C. Geibel, Valence effect on the thermopower of Eu systems, Phys. Rev. B 101 (2020) 235106, http://dx.doi.org/10.1103/PhysRevB.101.235106.

[40] R.C. Rau, The crystal structure of Eu_3O_4, "Acta Crystallographica" 20 (6) (1966) 716–723, http://dx.doi.org/10.1107/S0365110X66001737.

[41] S. Schulz, I.A. Nechaev, M. Güttler, G. Poelchen, A. Generalov, S. Danzenbächer, A. Chikina, S. Seiro, K. Kliemt, A.Y. Vyazovskaya, T.K. Kim, P. Dudin, E.V. Chulkov, C. Laubschat, E.E. Krasovskii, C. Geibel, C. Krellner, K. Kummer, D.V. Vyalikh, Emerging 2D-ferromagnetism and strong spin-orbit coupling at the surface of valence-fluctuating $EuIr_2Si_2$, "Npj Quantum Mater." 4 (2019) 26, http://dx.doi.org/10.1038/s41535-019-0166-z.

[42] B. Johansson, Valence state at the surface of rare-earth metals, Phys. Rev. B 19 (1979) 6615–6619, http://dx.doi.org/10.1103/PhysRevB.19.6615.

[43] W.D. Schneider, C. Laubschat, G. Kalkowski, J. Haase, A. Puschmann, Surface effects in Eu intermetallics: A resonant photoemission study, Phys. Rev. B 28 (1983) 2017–2022, http://dx.doi.org/10.1103/PhysRevB.28.2017.

[44] S. Engel, E.C.J. Gießelmann, R. Pöttgen, O. Janka, Trivalent europium - a scarce case in intermetallics, Rev. Inorg. Chem. 43 (4) (2023) 571–582, http://dx.doi.org/10.1515/revic-2023-0003.

[45] I. Horcas, R. Fernández, J.M. Gómez-Rodríguez, J. Colchero, J. Gómez-Herrero, A.M. Baro, WSXM: A software for scanning probe microscopy and a tool for nanotechnology, Rev. Sci. Instrum. 78 (1) (2007) 013705, http://dx.doi.org/10.1063/1.2432410.

[46] S. Fedoseenko, D. Vyalikh, I. Iossifov, R. Follath, S. Gorovikov, R. Püttner, J.-S. Schmidt, S. Molodtsov, V. Adamchuk, W. Gudat, G. Kaindl, Commissioning results and performance of the high-resolution Russian–German Beamline at BESSY II, Nucl. Instrum. Methods Phys. Res. Sect. A: Accel. Spectrometers, Detect. Assoc. Equip. 505 (3) (2003) 718–728, http://dx.doi.org/10.1016/S0168-9002(03)00624-7.

[47] A.M.I. Bakhit, et al., See supplemental material at [url will be inserted by publisher] for additional figures (figs. s1–s5), derivations, and supporting data, 2026.

[48] J.P. Baltrus, M.J. Keller, Rare earth oxides Eu_2O_3 and Nd_2O_3 analyzed by XPS, Surf. Sci. Spectra 26 (1) (2019) 014001, http://dx.doi.org/10.1116/1.5085768.

[49] J.-G. Kang, Y. Jung, B.-K. Min, Y. Sohn, Full characterization of $Eu(OH)_3$ and Eu_2O_3 nanorods, Appl. Surf. Sci. 314 (2014) 158–165, http://dx.doi.org/10.1016/j.apsusc.2014.06.165.

[50] F. Bertran, T. Gourieux, G. Krill, M. Alnot, J. Ehrhardt, W. Felsch, Growth of Eu on Pd(111): AES, photoemission and RHEED studies, Surf. Sci. Lett. 245 (1) (1991) L163–L169, http://dx.doi.org/10.1016/0167-2584(91)90792-P.

[51] F.H. Farwick zum Hagen, D.M. Zimmermann, C.C. Silva, C. Schlueter, N. Atodiresei, W. Jolie, A.J. Martínez-Galera, D. Dombrowski, U.A. Schröder, M. Will, P. Lazić, V. Caciuc, S. Blügel, T.-L. Lee, T. Michely, C. Busse, Structure and growth of hexagonal boron nitride on Ir(111), ACS Nano 10 (12) (2016) 11012–11026, http://dx.doi.org/10.1021/acsnano.6b05819.

[52] M. Ormaza, L. Fernández, M. Ilyn, A. Magaña, B. Xu, M.J. Verstraete, M. Gastaldo, M.A. Valbuena, P. Gargiani, A. Mugarza, A. Ayuela, L. Vitali, M. Blanco-Rey, F. Schiller, J.E. Ortega, High temperature ferromagnetism in a $GdAg_2$ monolayer, Nano Lett. 16 (7) (2016) 4230–4235, http://dx.doi.org/10.1021/acs.nanolett.6b01197.

[53] Y. Que, Y. Zhuang, Z. Liu, C. Xu, B. Liu, K. Wang, S. Du, X. Xiao, Two-Dimensional Rare Earth–Gold Intermetallic Compounds on Au(111) by Surface Alloying, J. Phys. Chem. Lett. 11 (10) (2020) 4107–4112, http://dx.doi.org/10.1021/acs.jpclett.0c00981.

[54] C. Xu, K. Bao, Y. Que, Y. Zhuang, X. Shao, K. Wang, J. Zhu, X. Xiao, A two-dimensional $ErCu_2$ intermetallic compound on Cu(111) with moiré-pattern-modulated electronic structures, "Phys. Chem. Chem. Phys." 22 (2020) 1693–1700, http://dx.doi.org/10.1039/C9CP05585A.

[55] L. Fernández, M. Blanco-Rey, R. Castrillo-Bodero, M. Ilyn, K. Ali, E. Turco, M. Corso, M. Ormaza, P. Gargiani, M.A. Valbuena, A. Mugarza, P. Moras, P.M. Sheverdyaeva, A.K. Kundu, M. Jugovac, C. Laubschat, J.E. Ortega, F. Schiller, Influence of 4f filling on electronic and magnetic properties of rare earth-au surface compounds, "Nanoscale" 12 (2020) 22258–22267, http://dx.doi.org/10.1039/D0NR04964F.

[56] M. Ormaza, L. Fernández, S. Lafuente, M. Corso, F. Schiller, B. Xu, M. Diakhate, M.J. Verstraete, J.E. Ortega, $LaAu_2$ and $CeAu_2$ surface intermetallic compounds grown by high-temperature deposition on Au(111), Phys. Rev. B 88 (2013) 125405, http://dx.doi.org/10.1103/PhysRevB.88.125405.

[57] M. Corso, L. Fernández, F. Schiller, J.E. Ortega, Au(111)-based nanotemplates by Gd alloying, ACS Nano 4 (3) (2010) 1603–1611, http://dx.doi.org/10.1021/nn901345s.

[58] M. Corso, M.J. Verstraete, F. Schiller, M. Ormaza, L. Fernández, T. Greber, M. Torrent, A. Rubio, J.E. Ortega, Rare-earth surface alloying: A new phase for $GdAu_2$, Phys. Rev. Lett. 105 (2010) 016101, http://dx.doi.org/10.1103/PhysRevLett.105.016101.

[59] R. Pöttgen, R.-D. Hoffmann, M.H. Möller, G. Kotzyba, B. Künnen, C. Rosenhahn, B.D. Mosel, Syntheses, crystal structures, and properties of EuRhIn, $EuIr_2$, and $EuIrSn_2$, J. Solid State Chem. 145 (1) (1999) 174–181, http://dx.doi.org/10.1006/jssc.1999.8236.

[60] C. Tomuschat, H.-U. Schuster, Magnetic properties of the compound series EuBX with B=element of the first subgroup and X=element of the fifth main group, Z. Anorg. Allg. Chem. 518 (11) (1984) 161–167, http://dx.doi.org/10.1002/zaac.19845181116.

[61] R.L. Johnston, R. Hoffmann, Structure-bonding relationships in the laves phases, Z. Anorg. Allg. Chem. 616 (10) (1992) 105–120, http://dx.doi.org/10.1002/zaac.19926161017.

[62] R.M. Bozorth, B.T. Matthias, H. Suhl, E. Corenzwit, D.D. Davis, Magnetization of compounds of rare [E]arths with [P]latinum [M]etals, Phys. Rev. 115 (1959) 1595–1596, http://dx.doi.org/10.1103/PhysRev.115.1595.

[63] S. Wieling, S.L. Molodtsov, C. Laubschat, G. Behr, Electronic and crystalline structure of epitaxial $EuNi_x$ films grown on Ni(111), Phys. Rev. B 65 (2002) 075415, http://dx.doi.org/10.1103/PhysRevB.65.075415.

[64] S. Wieling, S.L. Molodtsov, T. Gantz, J.J. Hinarejos, C. Laubschat, M. Richter, Surface compounds of divalent rare-earth metals with palladium, Phys. Rev. B 58 (1998) 13219–13223, http://dx.doi.org/10.1103/PhysRevB.58.13219.
[65] F. Schulz, R. Drost, S.K. Hämäläinen, T. Demonchaux, A.P. Seitsonen, P. Liljeroth, Epitaxial hexagonal boron nitride on Ir(111): A work function template, Phys. Rev. B 89 (2014) 235429, http://dx.doi.org/10.1103/PhysRevB.89.235429.
[66] Q. Fu, X. Bao, Surface chemistry and catalysis confined under two-dimensional materials, "Chem. Soc. Rev." 46 (2017) 1842–1874, http://dx.doi.org/10.1039/C6CS00424E.
[67] L. Daukiya, M. Nair, M. Cranney, F. Vonau, S. Hajjar-Garreau, D. Aubel, L. Simon, Functionalization of 2D materials by intercalation, Prog. Surf. Sci. 94 (1) (2019) 1–20, http://dx.doi.org/10.1016/j.progsurf.2018.07.001.
[68] M. Petrović, U. Hagemann, M. Horn-von Hoegen, F.-J. Meyer zu Heringdorf, Microanalysis of single-layer hexagonal boron nitride islands on Ir(111), Appl. Surf. Sci. 420 (2017) 504–510, http://dx.doi.org/10.1016/j.apsusc.2017.05.155.
[69] A.L. Gibb, N. Alem, J.-H. Chen, K.J. Erickson, J. Ciston, A. Gautam, M. Linck, A. Zettl, Atomic resolution imaging of grain boundary defects in monolayer chemical vapor deposition-grown hexagonal boron nitride, J. Am. Chem. Soc. 135 (18) (2013) 6758–6761, http://dx.doi.org/10.1021/ja400637n.
[70] J. Cai, W. Jolie, C.C. Silva, M. Petrović, C. Schlueter, T. Michely, M. Kralj, T.-L. Lee, C. Busse, Modifying the geometric and electronic structure of hexagonal boron nitride on Ir(111) by Cs adsorption and intercalation, Phys. Rev. B 98 (2018) 195443, http://dx.doi.org/10.1103/PhysRevB.98.195443.
[71] S. Doniach, M. Sunjic, Many-electron singularity in X-ray photoemission and X-ray line spectra from metals, J. Phys. C: Solid State Phys. 3 (2) (1970) 285, http://dx.doi.org/10.1088/0022-3719/3/2/010.
[72] D.A. Shirley, High-resolution X-Ray photoemission spectrum of the valence bands of gold, Phys. Rev. B 5 (1972) 4709–4714, http://dx.doi.org/10.1103/PhysRevB.5.4709.
[73] W.A. Dench, M.P. Seah, Quantitative Electron Spectroscopy of Surfaces: A Standard Data Base for Electron Inelastic Mean Free Path in Solids, Surf. Interf. Anal. 1 (1979) 1.
[74] K. Ueda, K. Suzuki, R. Toyoshima, Y. Monya, M. Yoshida, K. Isegawa, K. Amemiya, K. Mase, B.S. Mun, M.A. Arman, E. Grånäs, J. Knudsen, J. Schnadt, H. Kondoh, Adsorption and Reaction of CO and NO on Ir(111) Under Near Ambient Pressure Conditions, Top. Catal. 59 (2016) 487–496, http://dx.doi.org/10.1007/s11244-015-0523-5.
[75] S. Zhang, L. Yin, Q. Li, S. Wang, W. Wang, Y. Du, Laves phase Ir_2Sm intermetallic nanoparticles as a highly active electrocatalyst for acidic oxygen evolution reaction, "Chem. Sci." 14 (2023) 5887–5893, http://dx.doi.org/10.1039/D3SC01052J.
[76] R. Vercaemst, D. Poelman, L. Fiermans, R. Van Meirhaeghe, W. Laflère, F. Cardon, A detailed XPS study of the rare earth compounds EuS and EuF_3, J. Electron Spectrosc. Relat. Phenom. 74 (1) (1995) 45–56, http://dx.doi.org/10.1016/0368-2048(95)02349-6.
[77] C. Laubschat, B. Perscheid, W.D. Schneider, Final-state effects and surface valence in Eu—transition-metal compounds, Phys. Rev. B 28 (1983) 4342–4348, http://dx.doi.org/10.1103/PhysRevB.28.4342.
[78] W.-D. Schneider, C. Laubschat, I. Nowik, G. Kaindl, Shake-up excitations and core-hole screening in Eu systems, Phys. Rev. B 24 (1981) 5422–5425, http://dx.doi.org/10.1103/PhysRevB.24.5422.
[79] E.-J. Cho, S.-J. Oh, S. Imada, S. Suga, T. Suzuki, T. Kasuya, Origin of the high-binding-energy structure in the 3d core-level spectra of divalent Eu compounds, Phys. Rev. B 51 (1995) 10146–10149, http://dx.doi.org/10.1103/PhysRevB.51.10146.
[80] F. Orlando, R. Larciprete, P. Lacovig, I. Boscarato, A. Baraldi, S. Lizzit, Epitaxial growth of hexagonal boron nitride on Ir(111), J. Phys. Chem. C 116 (1) (2012) 157–164, http://dx.doi.org/10.1021/jp207571n.
[81] F. Orlando, P. Lacovig, L. Omiciuolo, N.G. Apostol, R. Larciprete, A. Baraldi, S. Lizzit, Epitaxial growth of a single-domain hexagonal boron nitride monolayer, ACS Nano 8 (12) (2014) 12063–12070, http://dx.doi.org/10.1021/nn5058968.
[82] A.B. Preobrajenski, A.S. Vinogradov, M.L. Ng, E. Ćavar, R. Westerström, A. Mikkelsen, E. Lundgren, N. Mårtensson, Influence of chemical interaction at the lattice-mismatched h−BN = Rh(111) and h−BN = Pt(111) interfaces on the overlayer morphology, Phys. Rev. B 75 (2007) 245412, http://dx.doi.org/10.1103/PhysRevB.75.245412.
[83] A. Fedorov, C.S. Praveen, N.I. Verbitskiy, D. Haberer, D. Usachov, D.V. Vyalikh, A. Nefedov, C. Wöll, L. Petaccia, S. Piccinin, H. Sachdev, M. Knupfer, B. Büchner, S. Fabris, A. Grüneis, Efficient gating of epitaxial boron nitride monolayers by substrate functionalization, Phys. Rev. B 92 (2015) 125440, http://dx.doi.org/10.1103/PhysRevB.92.125440.
[84] J.J. Yeh, I. Lindau, Atomic subshell photoionization cross section and asymmetry parameters: $1 \leq Z \leq 103$, At. D. Nucl. Data Tables 32 (1985) 1.
[85] M. Petrović, Sequential lithium deposition on hexagonal boron nitride monolayer on ir(111): Identifying intercalation and adsorption, Surf. Sci. 706 (2021) 121786, http://dx.doi.org/10.1016/j.susc.2020.121786.
[86] S. Ichinokura, A. Hemmi, H. Cun, K. Tanaka, R. Shimizu, T. Hitosugi, T. Greber, T. Hirahara, Efficiency of electron doping to monolayer hexagonal boron nitride by alkali metals, Appl. Phys. Lett. 122 (7) (2023) 071601, http://dx.doi.org/10.1063/5.0140074.
[87] P. Pervan, P. Lazić, M. Petrović, I. Šrut Rakić, I. Pletikosić, M. Kralj, M. Milun, T. Valla, Li adsorption versus graphene intercalation on Ir(111): From quenching to restoration of the Ir surface state, Phys. Rev. B 92 (2015) 245415, http://dx.doi.org/10.1103/PhysRevB.92.245415.
[88] W. Jolie, F. Craes, M. Petrović, N. Atodiresei, V. Caciuc, S. Blügel, M. Kralj, T. Michely, C. Busse, Confinement of Dirac electrons in graphene quantum dots, Phys. Rev. B 89 (2014) 155435, http://dx.doi.org/10.1103/PhysRevB.89.155435.
[89] R. Larciprete, S. Ulstrup, P. Lacovig, M. Dalmiglio, M. Bianchi, F. Mazzola, L. Hornekær, F. Orlando, A. Baraldi, P. Hofmann, S. Lizzit, Oxygen switching of the epitaxial graphene–metal interaction, ACS Nano 6 (11) (2012) 9551–9558, http://dx.doi.org/10.1021/nn302729j.